

Cobalt-Doped Hematite Thin Film for Electrocatalytic Water Oxidation in Highly Acidic Media

Wai Ling Kwong,^{a*} Cheng Choo Lee,^b Andrey Shchukarev,^c Johannes Messinger^{a,c*}

^aDepartment of Chemistry-Ångström Laboratory, Molecular Biomimetics, Uppsala University, 75120 Uppsala, Sweden

^bUmeå Core Facility for Electron Microscopy, Umeå University, 90187 Umeå, Sweden

^cDepartment of Chemistry, Kemiskt Biologiskt Centrum (KBC), Umeå University, 90187 Umeå, Sweden

*Corresponding authors: WaiLing.Kwong@kemi.uu.se; Johannes.Messinger@kemi.uu.se

Experimental Section

Chemicals

All chemicals were used without further purification: FeCl₃·6H₂O (≥99%; Sigma Aldrich), CoCl₂·6H₂O (98-102%; Acros Organics), Ti foil (99% metal basis; 0.127 mm thick; Alfa Aesar), and H₂SO₄ (95–97%; Merck).

Synthesis of catalyst-film electrodes

The monometallic FeO_y and CoO_y and bimetallic Co_xFe_{1-x}O_y catalyst films were deposited onto Ti foil substrate from the spray pyrolysis of 0.05 M metal chloride aqueous precursor. For the synthesis of Co_xFe_{1-x}O_y, the Co:Fe molar ratio of the precursor was adjusted to 1:4, 2:3, or 4:1. The spray nozzle was placed at 44 cm above and was tilted 45° with respect to the Ti foil, which was placed horizontally on a hotplate heated to a temperature of 400°C. Compressed air (0.5 bar) was used to carry the aerosol at a flow rate of 11.5 mL min⁻¹. The deposition was performed by multiple cycles of 4.5 min spraying to achieve a mass loading of ~1 mg cm⁻² (determined by a high-precision balance) in all films. Short break (~1 min) was taken between the cycles to allow the restoration of the hotplate temperature. Unless stated otherwise, the as-sprayed films were then annealed at 450°C for 30 min in air using a heating mantle.

Synthesis of IrO_y film electrodes

A 10 nm-thick Ir film was sputter-coated onto Ti foil substrate at an operating current of 20 mA for approximately 3 min. The Ir thickness was estimated by a film thickness monitor integrated in the metal sputter coater (Quorum Q150T ES). As reported in our recent work,¹ the as-prepared sample showed dominantly metallic nature. However, the sample was partially oxidized after being used for OER, therefore it is denoted as IrO_y in this work.

Characterizations

The mineralogical properties of the films were measured using powder X-ray diffraction (XRD; Bruker D5000; CuK_α radiation at 45 kV and 40 mA). Raman spectra were collected using a Renishaw inVia Raman microscope with a 20× objective lens and a 532 nm laser source. X-ray photoelectron spectra (XPS) were recorded using a Kratos Axis Ultra DLD spectrometer with a monochromatic AlK_α source. Scanning electron microscopy (SEM; 5 kV operating voltage) and elemental analysis were performed using a Carl Zeiss Merlin field-emission SEM with an energy-dispersive X-ray spectrometer (EDS; Oxford Instruments X-

Mas 80 mm²). Transmission electron microscopy (TEM) was performed using a FEI Titan Themis 200 with probe corrector and SuperX EDS. The crystal structural properties were examined by nano-beam diffraction (NBD) and scanning TEM (STEM). The lamella sample for TEM was prepared using a focused ion beam milling (FIB; FEI Strata DB235).

Electrochemical Measurements

A three-electrode electrochemical cell was used where the working, counter and reference electrodes consisting of the catalyst film, a Pt coil, and Ag/AgCl/1 M KCl were controlled using a potentiostat (Autolab PGSTAT302N). The uncoated side of the substrate with catalyst film was connected to a tinned copper wire using graphite paste for electrical contact. The catalyst film was placed against an O-ring at an open hole of the cell where the film geometric area exposed to an electrolyte of 0.5 M H₂SO₄ (pH 0.3) was ~0.2 cm², as defined by the O-ring diameter. In specified cases, the pH of the electrolyte was adjusted to 2 using 1 M KOH. Polarization curves (cyclic voltammetry; CV) were measured at a scan rate of 10 mV s⁻¹, starting in the anodic direction and were presented in this work after 4 CV scans to achieve repeatable curves and to minimize the capacitive current. All applied potentials (E) reported herein were referred to the reversible hydrogen electrode (RHE) *via* E (vs. RHE) = E (vs. Ag/AgCl/1 M KCl) + 0.222 V + 0.059×pH and were corrected for uncompensated cell resistance, which was determined using electrochemical impedance spectroscopy (EIS). The EIS was done at an AC potential with an amplitude of 20 mV and at frequencies ranging between 100 kHz and 0.1 Hz. The frequency of the AC potential was fixed at 2 kHz for the measurements of the capacitances in Mott-Schottky plots, which were done in 1 M KOH (pH 14) owing to the instability of the films under the measurement condition at pH 0.3.

The electrochemically active surface area (EASA) of the films were determined by measuring the double-layer capacitance (C) using CV at scan rates of 20-100 mV s⁻¹ at the open-circuit potential (OCP) ± 50 mV. The slope of the plot of $\Delta j/2$ (Δj is the difference between the anodic and the cathodic current densities at the OCP) as a function of scan rate yielded the value for C , which was compared to the capacitance of a flat surface (0.04 mF cm⁻²) for the estimation of EASA.²⁻⁴

The O₂ evolved during OER was quantified using membrane-inlet mass spectrometry (MIMS). This was done by analyzing the gaseous aliquots taken from the headspace of a sealed electrochemical cell that housed separately the working with reference electrodes and the counter electrode. The MIMS response toward the O₂ was calibrated using known amounts of air. The sum of the O₂ in the cell headspace and in the electrolyte (Henry constant of 0.013 mmol m⁻³ Pa⁻¹ for O₂)⁵ yielded the quantity of evolved O₂. Comparing this value with the quantity of O₂ calculated based on the assumption of a complete charge-to-O₂ conversion *via* a 4-electron oxidation yielded the reported Faradaic efficiency of the film.

Table S1. Summary of elemental analyses of $\text{Co}_x\text{Fe}_{1-x}\text{O}_y$.

Sample	Co content (Co/(Co+Fe))	
	SEM-EDS	XPS
FeO_y	0.00	0.00
$\text{Co}_{0.02}\text{Fe}_{0.98}\text{O}_y$	0.03	0.02
$\text{Co}_{0.05}\text{Fe}_{0.95}\text{O}_y$	0.07	0.05
$\text{Co}_{0.12}\text{Fe}_{0.88}\text{O}_y$	0.12	0.12
CoO_y	1.00	1.00

Table S2. Surface-adsorbed OH-to-lattice O peak area ratios obtained from the XPS O 1s data in Figure 3 and Figure S6c.

Sample	OH-to-lattice O peak area ratio
FeO_y	0.20
$\text{Co}_{0.02}\text{Fe}_{0.98}\text{O}_y$	0.33
$\text{Co}_{0.05}\text{Fe}_{0.95}\text{O}_y$	0.28
$\text{Co}_{0.12}\text{Fe}_{0.88}\text{O}_y$	0.32

All $\text{Co}_x\text{Fe}_{1-x}\text{O}_y$ show surface-adsorbed OH-to-lattice O peak area ratios that are higher than that of FeO_y , indicating that O vacancies form as a result of ionic charge compensation upon the aliovalent Co doping in hematite phase of the $\text{Co}_x\text{Fe}_{1-x}\text{O}_y$. The absence of uptrend in these ratios among the $\text{Co}_x\text{Fe}_{1-x}\text{O}_y$ may be due to a competing charge compensation mechanism via electron-hole formation (*i.e.*, electronic compensation), which occurs at moderate Co doping levels.

Table S3. Comparison of the OER activity of noble-metal-free catalysts in acidic electrolyte.

Sample/(substrate)	pH	Overpotential @ $j = 10 \text{ mA cm}^{-2}$ [mV]	Stability	Ref.
$\text{Co}_{0.05}\text{Fe}_{0.95}\text{O}_y$ /(Ti foil)	0.3	650	50 h @ $j = 10 \text{ mA cm}^{-2}$	This work
	2	650	85 h @ $j = 10 \text{ mA cm}^{-2}$	
F-doped $\text{Cu}_{1.5}\text{Mn}_{1.5}\text{O}_4$ /(Ti foil)	0.3	320	24 h @ $j = 16 \text{ mA cm}^{-2}$	6
Amorphous carbon-coated Co_3O_4 /(CP)	0.3	370	87 h @ $j = 100 \text{ mA cm}^{-2}$	7
1T- MoS_2 /(CP)	0.3	420	2 h @ $j = 10 \text{ mA cm}^{-2}$	8
Surface-modified AISI Ni 42 steel sheet	0	445	6 h @ $j = 10 \text{ mA cm}^{-2}$	9
	1	552	42 h @ $j = 10 \text{ mA cm}^{-2}$	
Nanocrystalline Co_3O_4 /(FTO)	0.3	570	12 h @ $j = 10 \text{ mA cm}^{-2}$	10
$\text{Mn}_x\text{Sb}_{1-x}\text{O}_z$ /(Pt/Ti/SiO ₂ /Si)	0	580	30 h @ $\eta = 586 \text{ mV}$	11
$\text{Ni}_{0.5}\text{Mn}_{0.5}\text{Sb}_{1.7}\text{O}_y$ /(ATO-coated quartz)	0	670	168 h @ $j = 10 \text{ mA cm}^{-2}$	12
Ag-doped CO_3O_4 /(FTO)	0.3	680	10 h @ $\eta = 370 \text{ mV}$	13
Ti- MnO_2 /(Au-coated quartz)	1.3	>670	2 h @ $j \sim 7 \text{ mA cm}^{-2}$	14
CoFePbO_x /(FTO)	2	>700	50 h @ $j = 1 \text{ mA cm}^{-2}$	15

CP: carbon paper; FTO: F-doped tin oxide; ATO: Sb-doped tin oxide.

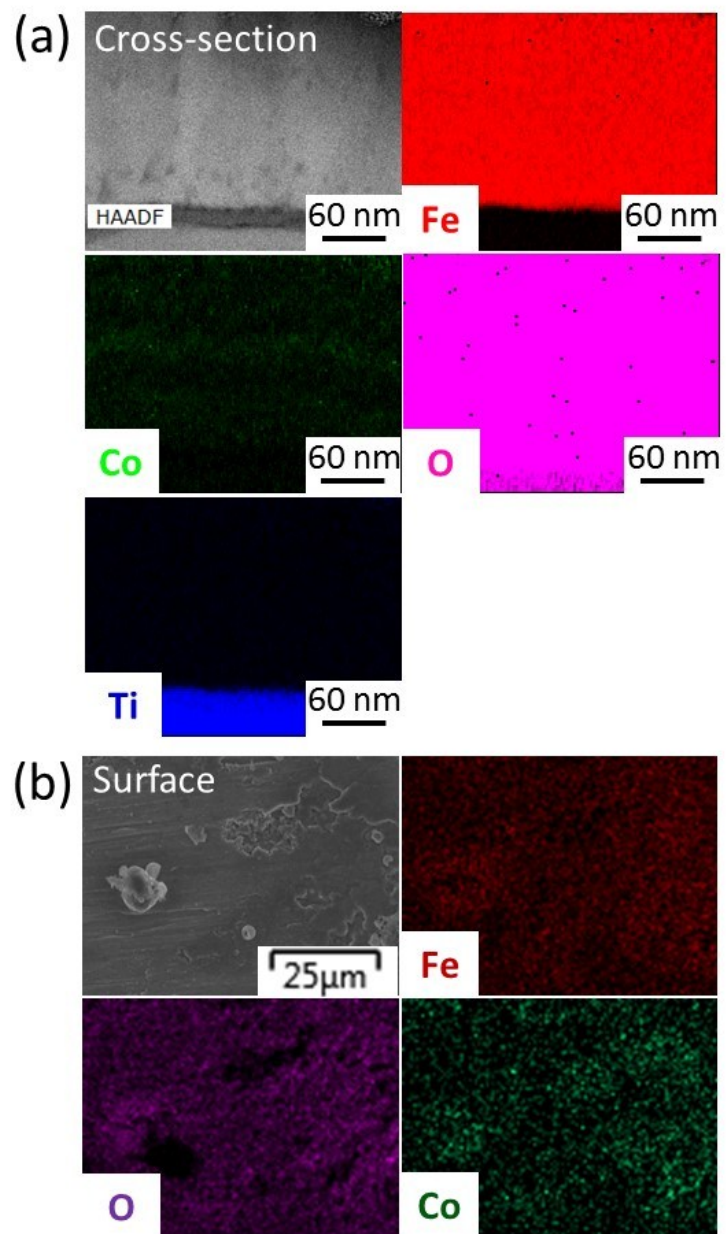


Figure S1. Elemental mapping of $\text{Co}_{0.05}\text{Fe}_{0.95}\text{O}_y$ by (a) TEM-EDS and (b) SEM-EDS.

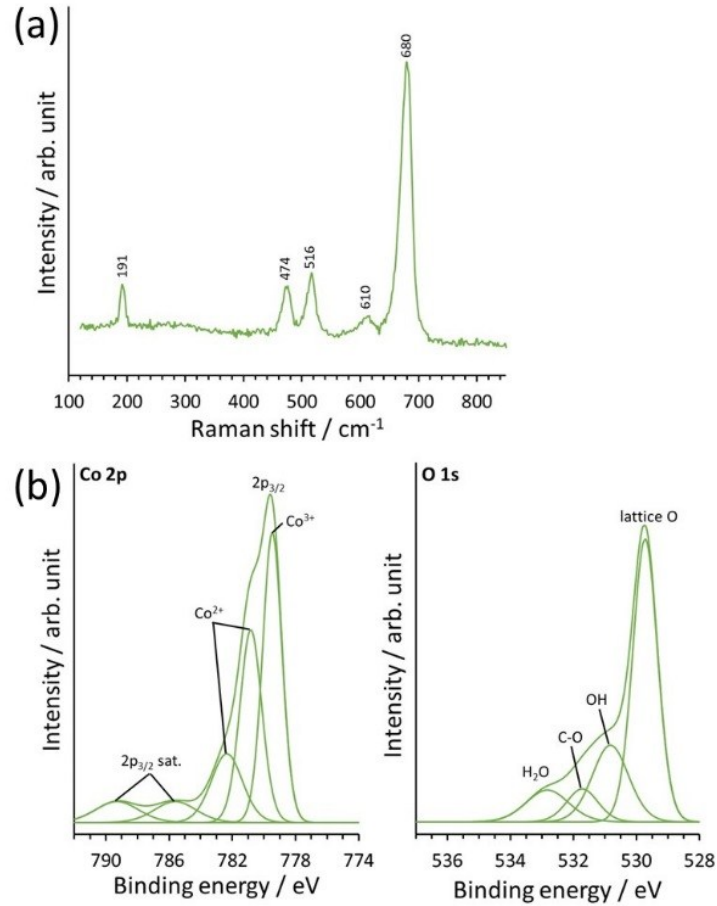


Figure S2. (a) Raman spectrum of CoO_y showing the characteristic Co_3O_4 bands.¹⁶ (b) High-resolution XPS spectra of CoO_y . In the Co 2p region, the CoO_y exhibits characteristic Co_3O_4 2p_{3/2} peaks at 779.5 (Co^{3+}) and 780.8 eV (Co^{2+}), as well as the satellite peaks at 785.6 (Co^{2+}) and 789.3 eV (Co^{3+}).^{17, 18} A peak due to the Co^{2+} in $\text{Co}(\text{OH})_2$ is located at 782.4 eV.¹⁸ In the O 1s region, the peak due to lattice O^{2-} of the oxide structures is spotted at 529.7 eV.¹⁷ Other O 1s peaks at 530.8-533.5 eV are due to the surface-adsorbed O species, *i.e.*, hydroxyl species, oxygenated carbon and water molecules.^{19, 20}

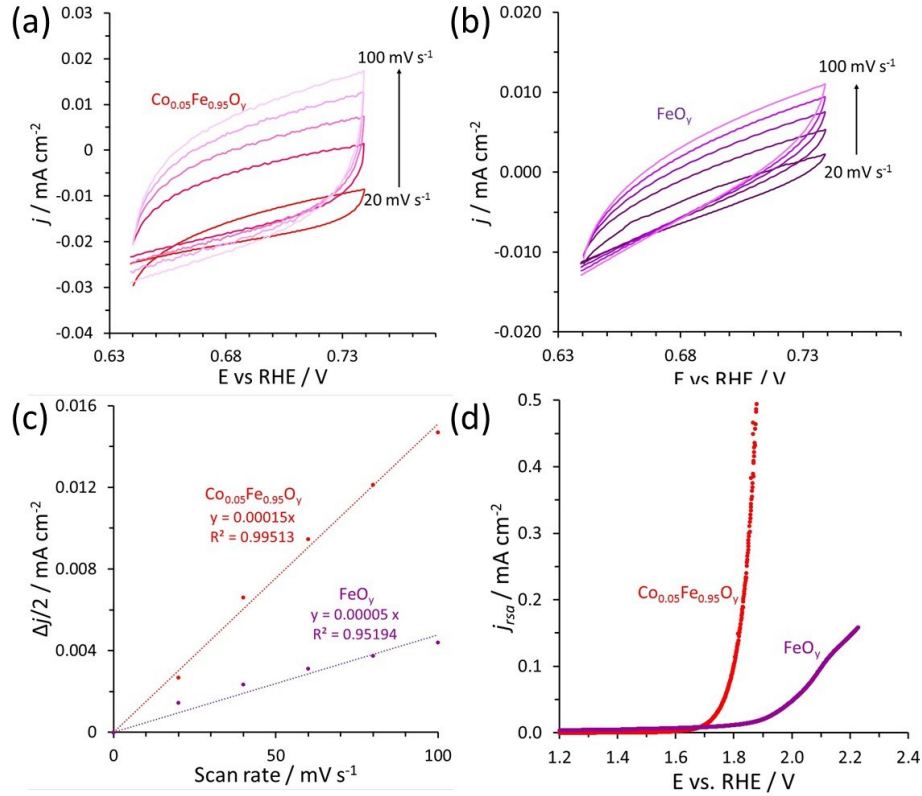


Figure S3. CV scans of (a) $\text{Co}_{0.05}\text{Fe}_{0.95}\text{O}_y$ and (b) FeO_y at rates 20-100 mV s^{-1} in the non-Faradaic potential region. (c) $\Delta j/2$ as a function of scan rate. Δj is the difference between the anodic and the cathodic current densities at the open-circuit potential, *viz.*, 0.69 V vs. RHE, from (a,b). The slopes of the plots give the values for capacitance C of the films. Their comparison with that of flat surfaces ($C = 0.04 \text{ mF cm}^{-2}$)²⁻⁴ shows that the surfaces of FeO_y ($C = 0.05 \text{ mF cm}^{-2}$) and $\text{Co}_{0.05}\text{Fe}_{0.95}\text{O}_y$ ($C = 0.15 \text{ mF cm}^{-2}$) exhibit 1.3 and 3.8 times higher roughness, respectively. (d) Polarization curves in which the current is normalized to the sample real surface area.

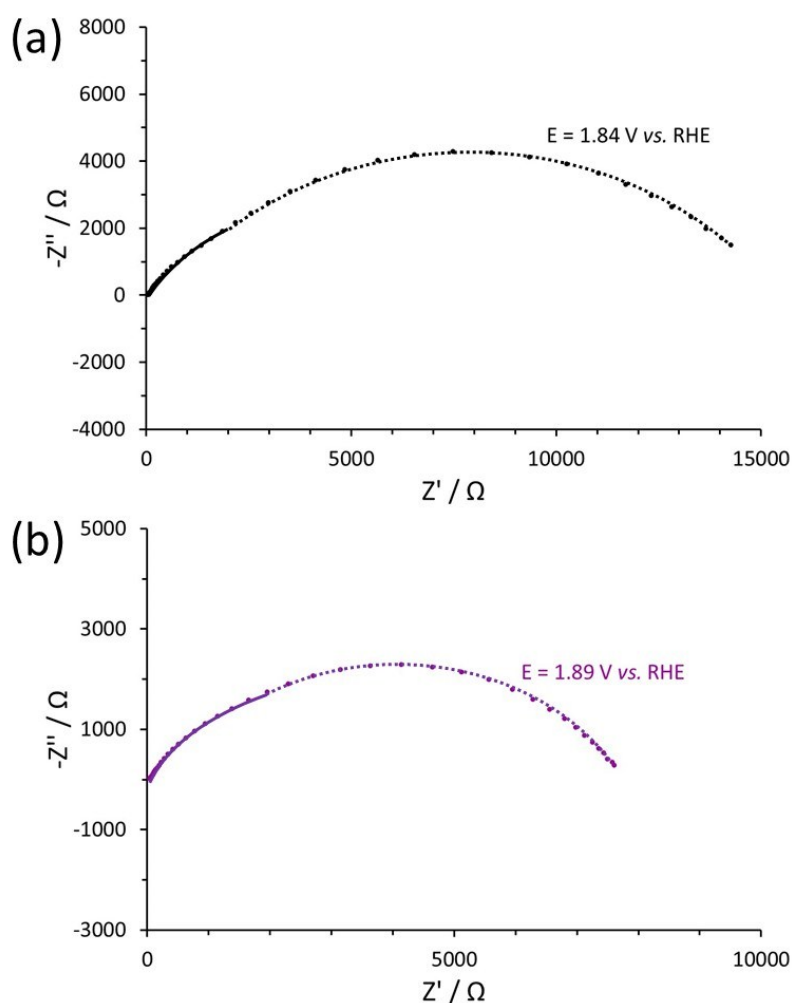


Figure S4. Two Nyquist plots of FeO_y obtained at (a) $E = 1.84$ V vs. RHE and (b) 1.89 V vs. RHE. For each plot, two closely overlapped semicircles are observed, where the one in the low- (dotted line) and high-frequency (solid line) region (*i.e.*, the high- and low- Z' region) are attributed to the resistance of charge transfer at the film-electrolyte interface and across the film, respectively.

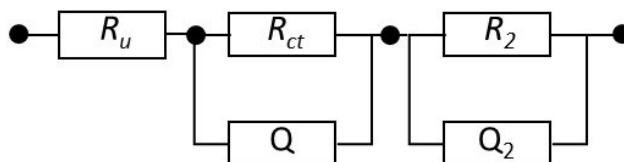


Figure S5. The equivalent circuit model used to fit the EIS data. R_u is the uncompensated series resistance; R_{ct} and Q are the charge transfer resistance and the constant phase element, respectively, at the film/electrolyte interface; R_2 and Q_2 are the charge transfer resistance and the constant phase element, respectively, across the film.

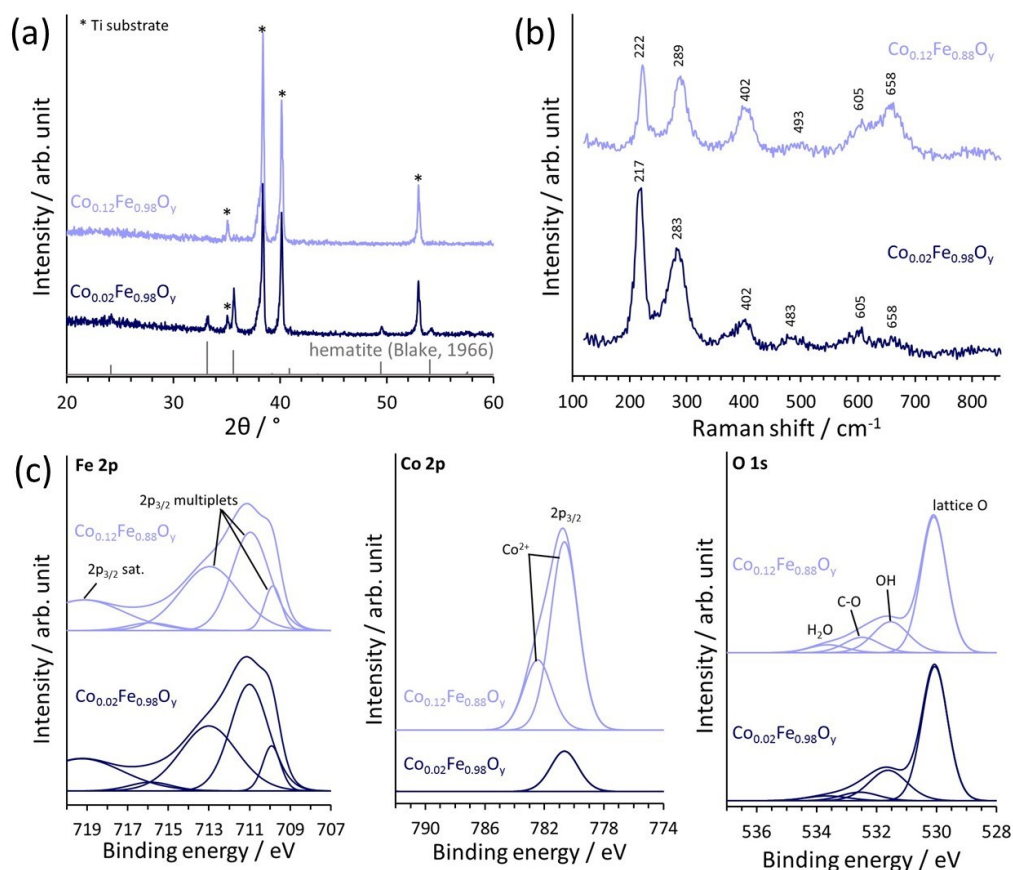


Figure S6. (a) XRD, (b) Raman and (c) high-resolution XPS spectra of $\text{Co}_{0.02}\text{Fe}_{0.98}\text{O}_y$ and $\text{Co}_{0.12}\text{Fe}_{0.88}\text{O}_y$.

Only XRD peaks that are due to $\alpha\text{-Fe}_2\text{O}_3$ are observed in $\text{Co}_{0.02}\text{Fe}_{0.98}\text{O}_y$ (Figure S6a). These peaks become lower in intensity and broader in $\text{Co}_{0.12}\text{Fe}_{0.88}\text{O}_y$, indicating a declining degree of crystallinity that may be attributed to a decreasing grain or crystallite size. The Raman spectra show characteristic $\alpha\text{-Fe}_2\text{O}_3$ bands (Figure S6b),²¹ in agreement with the XRD results. A core XPS peak of Fe^{3+} $2p_{3/2}$ at the binding energy of 711.0 eV and corresponding multiplets at 709.9–713.1 eV (Figure S6c), are attributed to the presence of hematite.²² The Co dopant in $\text{Co}_{0.02}\text{Fe}_{0.98}\text{O}_y$ and $\text{Co}_{0.12}\text{Fe}_{0.88}\text{O}_y$ presents as Co^{2+} , as evidenced by the peak at 780.8 eV, as well as the peak at 782.4 eV for the $\text{Co}_{0.12}\text{Fe}_{0.88}\text{O}_y$.^{17, 18} Both films show an O 1s peak due to lattice O^{2-} of the oxide structures at 530.1 eV.^{17, 23} Other O 1s peaks at 530.8–533.5 eV are due to the surface-adsorbed O species, *i.e.*, hydroxyl species, oxygenated carbon and water molecules.^{19, 20}

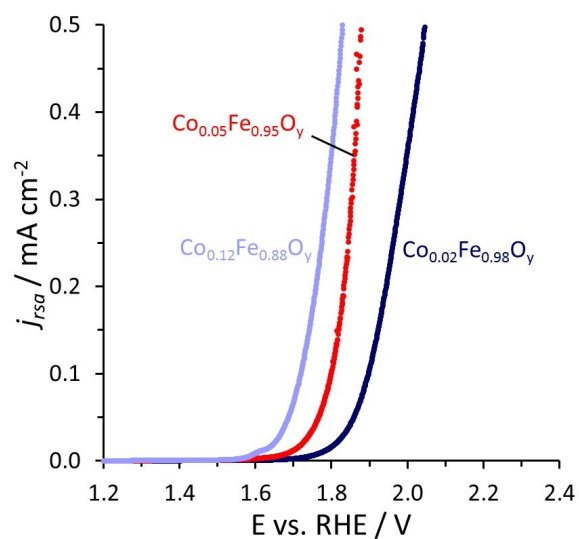


Figure S7. Polarization curves in which the current is normalized to the sample real surface area.

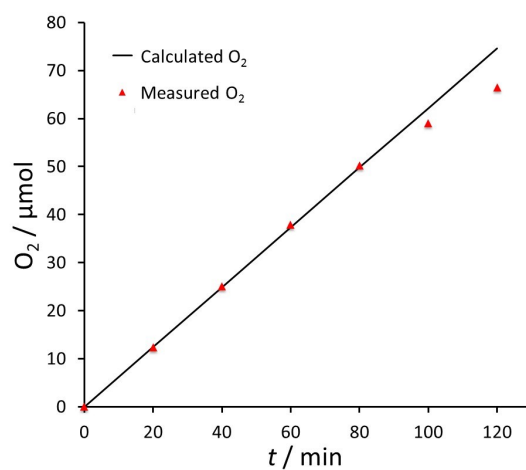


Figure S8. Faradaic efficiency measurement at $j = 10 \text{ mA cm}^{-2}$ using $\text{Co}_{0.05}\text{Fe}_{0.95}\text{O}_y$.

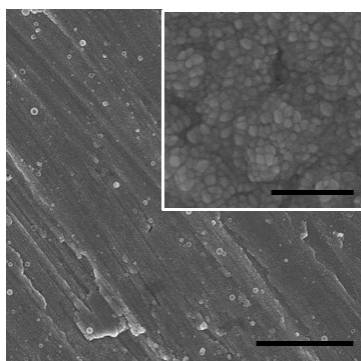


Figure S9. Top-view SEM images of $\text{Co}_{0.12}\text{Fe}_{0.88}\text{O}_y$. Scale bars: $2 \mu\text{m}$; inset 200 nm .

References

1. W. L. Kwong, C. C. Lee, A. Shchukarev, E. Björn and J. Messinger, *J. Catal.*, 2018, **365**, 29-35.
2. D. C. Grahame, *Chem. Rev.*, 1947, **41**, 441–501.
3. R. Kötz and M. Carlen, *Electrochem. Acta*, 2000, **45**, 2483–2498.
4. B. E. Conway and B. V. Tilak, *Electrochem. Acta*, 2002, **47**, 3571–3594.
5. R. Sander, *Atmos. Chem. Phys.*, 2015, **15**, 4399–4981.
6. P. P. Patel, M. K. Datta, O. I. Velikokhatnyi, R. Kuruba, K. Damodaran, P. Jampani, B. Gattu, P. M. Shanthi, S. S. Damle and P. N. Kumta, *Sci. Rep.*, 2016, **6**, 28367.
7. X. Yang, H. Li, A.-Y. Lu, S. Min, Z. Idriss, M. N. Hedhili, K.-W. Huang, H. Idriss and L.-J. Li, *Nano Energy*, 2016, **25**, 42–50.
8. J. Wu, M. Liu, K. Chatterjee, K. P. Hackenberg, J. Shen, X. Zou, Y. Yan, J. Gu, Y. Yang, J. Lou and P. M. Ajayan, *Adv. Mater. Interfaces*, 2016, **3**, 1500669.
9. H. Schäfer, K. Küpper, M. Schmidt, K. Müller-Buschbaum, J. Stangl, D. Daum, M. Steinhart, C. Schulz-Kölbel, W. Han, J. Wollschläger, U. Krupp, P. Hou and X. Liu, *Catal. Sci. Technol.*, 2018, **8**, 2104-2116
10. J. S. Mondschein, J. F. Callejas, C. G. Read, J. Y. C. Chen, C. F. Holder, C. K. Badding and R. E. Schaak, *Chem. Mater.*, 2017, **29**, 950–957.
11. L. Zhou, A. Shinde, J. H. Montoya, A. Singh, S. Gul, J. Yano, Y. Ye, E. J. Crumlin, M. H. Richter, J. K. Cooper, H. S. Stein, J. A. Haber, K. A. Persson and J. M. Gregoire, *ACS Catal.*, 2018, **8**, 10938–10948.
12. I. A. Moreno-Hernandez, C. A. MacFarland, C. G. Read, K. M. Papadantonakis, B. S. Brunshwig and N. S. Lewis, *Energy Environ. Sci.*, 2017, **10**, 2103-2108.
13. K.-L. Yan, J.-Q. Chi, J.-Y. Xie, B. Dong, Z.-Z. Liu, W.-K. Gao, J.-H. Lin, Y.-M. Chai and C.-G. Liu, *Renew. Energy*, 2018, **119** 54-61.
14. R. Frydendal, E. A. Paoli, I. Chorkendorff, J. Rossmeisl and I. E. L. Stephens, *Adv. Energy Mater.*, 2015 **5**, 1500991.
15. M. Huynh, T. Ozel, C. Liu, E. C. Lau and D. G. Nocera, *Chem. Sci.*, 2017, **8**, 4779–4794.
16. V. G. Hadjiev, M. N. Iliev and I. V. Vergilov, *J. Phys. C: Solid State Phys.*, 1988, **21** L199-L201.
17. S. C. Petitto and M. A. Langell, *J. Vac. Sci. Technol. A*, 2004, **22**, 1690-1696.
18. M. C. Biesinger, B. P. Payne, A. P. Grosvenor, L. W. M. Lau, A. R. Gerson and R. S. C. Smart, *Appl. Surf. Sci.*, 2011, **257**, 2717-2730.
19. S. Yamamoto, T. Kendelewicz, J. T. Newberg, G. Ketteler, D. E. Starr, E. R. Mysak, K. J. Andersson, H. Ogasawara, H. Bluhm, M. Salmeron, G. E. Brown and A. Nilsson, *J. Phys. Chem. C*, 2010, **114**, 2256–2266.
20. Y. Zhang, K. Dong, Z. Liu, H. Wang, S. Ma, A. Zhang, M. Li, L. Yu and Y. Li, *Prog. Nat. Sci. Mater. Int.*, 2017, **27**, 443-451.
21. N. M. A. Rashid, C. Haw, W. Chiu, N. H. Khanis, A. Rohaizad, P. Khiew and S. A. Rahman, *CrystEngComm*, 2016 **18**, 4720–4732.
22. A. P. Grosvenor, B. A. Kobe, M. C. Biesinger and N. S. McIntyre, *Surf. Interface Anal.*, 2004, **36**, 1564–1574.
23. R. M. Cornell and U. Schwertmann, *The Iron Oxides. Structure, Properties, Reactions, Occurrences and Uses*, Wiley-VCH, Weinheim, 2003.